The Astrophysical Journal, 977:42 (8pp), 2024 December 10 https://doi.org/10.3847/1538-4357/ad8dce
© 2024. The Author(s). Published by the American Astronomical Society.
OPEN ACCESS

Neutrino Detection Rates from Lepto-hadronic Model Simulations of Bright Blazar Flares

Joshua Robinson and Markus Böttcher
Centre for Space Research, North-West University, Potchefstroom, 2520, South Africa
Received 2024 July 26; revised 2024 October 11; accepted 2024 October 24; published 2024 December 2

Abstract

There is mounting evidence that blazars are the sources of part of the very-high-energy astrophysical neutrino flux detected by IceCube. In particular, there have been several spatial and temporal coincidences of individual IceCube neutrino events with flaring blazars, the most prominent of them being IceCube-170922A, coincident with a multiwavelength flare of TXS 0506+056. Motivated by this, we used the time-dependent lepto-hadronic code OneHaLe to model the spectral energy distributions and light curves of a sample of bright γ-ray flares of blazars detected by Fermi-Large Area Telescope, for which Kreter et al. provided calorimetric estimates of the expected neutrino detection rates. Flares were modeled with temporal changes of the proton injection spectra. Our analysis shows that the calorimetric approach overestimates the increase in neutrino production by a factor of typically $\sim$10 if the γ-ray emission is dominated by proton-synchrotron radiation.

Unified Astronomy Thesaurus concepts: Blazars (164); Neutrino astronomy (1100); Active galactic nuclei (16); Gamma-ray astronomy (628)

1. Introduction

The sources of very-high-energy and ultra-high-energy cosmic rays remain unclear, with several plausible candidate source classes suggested that fulfill the Hillas criterion (A. M. Hillas & M. Hillas 1984). The sites where cosmic rays are accelerated would also produce neutrinos due to the interaction between cosmic rays and either radiation fields or matter. These neutrinos may be used to locate where the acceleration is taking place as the weak interaction cross sections coupled with the charge neutrality of neutrinos allow them to travel through both matter and magnetic fields without absorption or deflection (T. K. Gaisser et al. 1996). The jets of active galactic nuclei (AGNs) offer a suitable site for the acceleration of such high-energy neutrinos (e.g., K. Mannheim et al. 1992) as the high luminosity within an emission region of relatively compact size provides a dense target photon field for photo–pion interactions and hence a suitable environment for photo–pion-induced neutrino production. Analyses have, however, shown that γ-ray bright blazars are unlikely to be the dominant source of the diffuse neutrino flux detected by IceCube (e.g., K. Murase et al. 2018). Work by K. Yoshida et al. (2023) also shows that, even with flaring states taken into account, blazars cannot account for the bulk of the IceCube neutrino flux. Evidence of a spatial correlation between neutrinos and γ-ray-loud (e.g., S. Garrappa et al. 2019; S. Buson et al. 2022) blazars, as well as radio-loud, core-dominated blazars (e.g., A. Plavin et al. 2020; A. V. Plavin et al. 2021, 2023) is mounting, and there have been numerous tentative associations of individual IceCube neutrino events with multiwavelength flaring blazars. Most prominently, in 2017, IceCube detected a 290 TeV neutrino from the direction of the blazar TXS 0506+056 (M. Aartsen et al. 2018). At the time of the detection, TXS 0506+056 was in a state of increased γ-ray emission. Another remarkable example was the blazar PKS 0735+17, which was found in coincidence with not only the IceCube event IceCube-211208A, but potentially also neutrino detections by three other experiments (Baikal-GVD, Baksan, and KM3NeT) within about a week of the IceCube alert (A. Acharyya et al. 2023; N. Sahakyan et al. 2023). The active galaxy NGC 1068 was also identified as a source of astrophysical neutrinos detected by IceCube (R. Abbasi et al. 2022), further strengthening the link between AGN and neutrino production, though NGC 1068 is not a blazar, but rather a Seyfert II galaxy (C. K. Seyfert 1943).

In M. Kreter et al. (2020), neutrino detection rate expectations from a sample of the 50 brightest γ-ray flares of blazars (at the time) were calculated using a calorimetric approach developed in F. Kraußet al. (2014) and M. Kadler et al. (2016). In this work, we analyze the same flares as M. Kreter et al. (2020) using detailed physical simulations performed with the OneHaLe code (C. Diltz & M. Böttcher 2016; M. Zacharias 2021; M. Zacharias et al. 2022). Archival multiwavelength data were used to construct spectral energy distributions (SEDs) of the blazars in their quiescent state. These were modeled with OneHaLe in a time-independent equilibrium state. Fermi-Large Area Telescope (LAT) data were used to construct both light curves and SEDs of these blazars in flaring states. Where available, Swift X-ray Telescope(XRT) data were also used to provide additional contemporaneous SED and light-curve information. The flares were reproduced by perturbing the input parameters governing the proton injection spectrum and luminosity from the quiescent-state fits on a timescale similar to that of the length of the flares to simultaneously reproduce the flaring-state SEDs and the Fermi-LAT γ-ray light curves.

The structure of this paper is as follows. In Section 2 we outline the methods used to analyze each flare's data. Section 3 discusses the physical model used in calculating the SEDs and light curves of the blazars and the method to extract the expected number of neutrinos detected by IceCube and KM3NeT for each flare from these simulations. In Section 4 the results of the modeling are discussed.

Original content from this work may be used under the terms of the Creative Commons Attribution 4.0 licence. Any further distribution of this work must maintain attribution to the author(s) and the title of the work, journal citation and DOI.

2. Data Analysis

2.1. Swift XRT data

The data from the Swift XRT were reduced, calibrated, and cleaned using the XRT-PIPELINE in HEASOFT 6.15.1. Grades 0-12 were used for observations in photon counting mode and grade 0 for those in window-timing mode (M. Kreter et al. 2020). Spectral fitting was performed in XSPEC, using a power-law spectrum with absorption modeled by the Tübingen–Boulder interstellar medium absorption model, `tbabs` (J. Wilms et al. 2000). For this absorption, the photoelectric absorption cross sections of D. A. Verner et al. (1996) and relative abundances in J. Wilms et al. (2000) were used.

2.2. Fermi-LAT Data

All analysis of the Fermi-LAT data was performed using `fermipy v1.2` (M. Wood et al. 2018). The instrument response function used was `P8R2_SOURCE_V6`. The Galactic diffuse emission model `gll_iem_v07.fits` was used in conjunction with the isotropic diffuse model `iso_P8R3_SOURCE_V3_v1.txt`. As the variability of these flares was often less than 3 days the Fermi Lightcurve Repository proved unsuitable for use in this work as it does not have the required time resolution. All sources were fit according to their respective models in the 4FGL catalog (S. Abdollahi et al. 2020). For each flare listed in M. Kreter et al. (2020) starting on t_{min} (MJD) and ending on date t_{max} (MJD), a light curve was generated between $t_{min} - 1$ day and $t_{max} + 1$ day, using either 6, 12, or 24 hr binning depending on the length of the flare. An SED was then generated for the time bin within the range t_{min} to t_{max} with the highest photon flux between 100 MeV and 300 GeV.

3. Model Description

The calorimetric approach used in M. Kreter et al. (2020) estimates the integrated neutrino energy flux as directly proportional to the integrated γ-ray flux. Using this method, the maximum number of neutrinos a blazar flare can create is given by

$$N_\nu^{\max} = A_{\rm Eff} \cdot \left(\frac{\phi_\gamma}{E_\nu}\right) \cdot \Delta t. \tag{1}$$

Here ϕ_γ represents the integrated X-ray–γ-ray flux between 10 keV and 20 GeV, $A_{\rm Eff}$ the energy-dependent effective area of the IceCube detector, E_ν the energy of the neutrino, and Δt the duration of the flare. A flux of monoenergetic neutrinos with energy $E_\nu = 2$ PeV was used in M. Kreter et al. (2020) in order to be comparable to M. Kadler et al. (2016). The maximum number of neutrino events is then scaled down by an empirical factor of 0.025 in order to provide a more realistic estimate of neutrino events.

In this work, the blazar flares were simulated using OneHaLe, a code for a time-dependent one-zone lepto-hadronic blazar model. This code assumes a homogeneous, spherical emission region with a time-dependent injection of protons and electrons in power-law distributions, subject to a disordered magnetic field. To simulate this emission region the code solves the Fokker–Planck equation

$$\frac{\partial n_i(\gamma, t)}{\partial t} = \frac{\partial}{\partial \gamma}\left(\frac{\gamma^2}{(a+2)t_{\rm acc}}\frac{\partial n_i(\gamma, t)}{\partial \gamma}\right) - \frac{\partial}{\partial \gamma}(\dot{\gamma} \cdot n_i(\gamma, t)) + Q_i(\gamma, t) - \frac{n_i(\gamma, t)}{t_{\rm esc}} - \frac{n_i(\gamma, t)}{\gamma t_{\rm decay}} \tag{2}$$

for electrons, protons, muons, and charged pions. The first term on the right-hand side of Equation (2) accounts for second-order Fermi acceleration of the particles, while the second term accounts for first-order Fermi acceleration and radiative as well as adiabatic cooling. The injection of new particles is represented by the term $Q_i(\gamma, t)$. Terms four and five represent the escape and decay of particles, respectively. The term $\dot{\gamma}$ encompasses all energy losses resulting from radiative output and adiabatic cooling (see, e.g., M. Bottcher et al. 2012; M. Cerruti 2020; M. Zacharias 2021; M. Zacharias et al. 2022, for details).

Using archival data from the SSDC SED builder,[1] parameters were found to model all sources in their quiescent states. To decrease the number of free variables, values from the literature were incorporated where possible, and scaling relationships were used for the radii and luminosities of the broad-line region (BLR) and dusty torus (DT). Once an appropriate parameter set was found, this steady-state solution was then perturbed in order to reproduce the light curves observed by the Fermi-LAT. In conjunction with the light curves, the SEDs of the blazars at the point of maximum flux were also fitted. These perturbations are modeled using a modified version of the default OneHaLe perturbations. The perturbation is treated as an additional power-law proton spectrum injected alongside the existing proton injection spectrum. This additional power law has the form

$$Q'_p(\gamma, t) = Q'_{0,p}(t)\gamma^{-\alpha'_p} H(\gamma: \gamma'_{\rm min}, \gamma'_{\rm max}), \tag{3}$$

with $Q'_{0,p}(t)$ evolving as a symmetric Gaussian and H being the Heaviside function. Once the flare light curves and SEDs could be reproduced, the total number of observable neutrinos per time interval was calculated using the energy- and angle-dependent effective areas of IceCube (M. G. Aartsen et al. 2013) as well as the proposed energy-dependent effective areas of the completed KM3NeT (S. Adrián-Martinez et al. 2016) for the neutrino spectra of each flavor. This observable neutrino flux was integrated over the time intervals calculated using an asymmetric Gaussian and summed over flavors to calculate the total neutrino count for each flare.

The total number of neutrinos produced was then treated as the mean number of events in a Poisson distribution to calculate the probability of neutrinos from these flares being detected.

$$P_{\rm Det} = P(k \geqslant 1) = 1 - P(0) = 1 - e^{-N_\nu}, \tag{4}$$

where k is the number of neutrinos detected and N_ν is the total number of neutrinos expected.

[1] https://tools.ssdc.asi.it/SED/

3.1. Sources

To compare results with M. Kreter et al. (2020), the same sources were used in this work. Parameter values that could be sourced from the existing literature were used wherever possible to narrow down the number of free parameters, including the mass of the central black hole, the accretion disk luminosity, and details regarding the relativistic motion of the jet. For sources where parameter values could not be found, values similar to the other sources in the sample were used. For the distances from the central black hole to the sources of external radiation fields (BLR and DT), scaling relationships from G. Ghisellini & F. Tavecchio (2009) were used. These relate the radii of both the BLR and the DT as proportional to the square root of the luminosity of the accretion disk:

$$R_{\rm BLR} = 10^{17}\sqrt{L_{\rm AD,45}} \tag{5}$$

$$R_{\rm DT} = 2.5 \times 10^{18}\sqrt{L_{\rm AD,45}}, \tag{6}$$

where $L_{\rm AD,45}$ is the luminosity of the accretion disk in units of $10^{45}\,{\rm erg\,s^{-1}}$. The BLR and DT were both set to a luminosity of 10% of the accretion disk luminosity. The temperature of the DT was set at 2000 K, as any temperature above this would cause the dust to sublimate (G. Ghisellini & G. Ghisellini 2013). The temperature of the BLR was kept constant at 10^4 K following G. Ghisellini & G. Ghisellini (2013). The radius of the emission region is constrained by

$$R_{\rm blob} < \delta\frac{ct_{\rm var}}{1+z}, \tag{7}$$

where $t_{\rm var}$ is the flux-doubling timescale in the observer frame and the Doppler factor of the emission region is $\delta = (\Gamma[1 - \beta\cos\theta])^{-1}$. The size of the emission region can also be used to constrain the maximum energy of injected particles, as for a particle to be confined within the region, the Larmor radius of that particle must be smaller than the emission region size.

3.1.1. PKS 1510-089 (32 Flares)

PKS 1510-089 is an FSRQ located at a redshift of $z = 0.36$ (D. J. Thompson et al. 1990), with a black hole mass of $4.46 \times 10^8\,M_\odot$ (J. Woo & C. M. Urry 2002) and an accretion disk luminosity of $10^{46}\,{\rm erg\,s^{-1}}$ (G. Pucella et al. 2008). The viewing angle and bulk Lorentz factor (BLF) of the jet have been sourced from S. G. Jorstad et al. (2017) as $1.^\circ2$ and 22.5, respectively, giving a Doppler factor of $\delta = 37$. This makes this the fastest jet in the sample. Within the dates included in this sample, PKS 1510-089 is observed to have a doubling time of approximately 0.6 days, implying that the spherical emission region has a radius smaller than 4.2×10^{16} cm.

3.1.2. 3C 279 (10 Flares)

3C 279 is located at a redshift of $z = 0.53$ (P. Marziani et al. 1996). The mass of the central black hole is taken as $2.7 \times 10^8\,M_\odot$ (J. Woo & C. M. Urry 2002) along with an accretion disk luminosity of $2 \times 10^{45}\,{\rm erg\,s^{-1}}$ (E. Pian et al. 2005). The viewing angle and BLF of the jet have been sourced from S. G. Jorstad et al. (2017) as $1.^\circ9$ and 13.3, respectively, giving a Doppler factor of $\delta = 22$. A flux doubling time of 0.12 days has been observed in the γ-ray light curve of 3C 279. This implies that the spherical emission region must have a radius smaller than 4.5×10^{15} cm.

3.1.3. PKS 1424-41 (Three Flares)

PKS 1424-41 is located at redshift $z = 1.52$ (M. T. Murphy et al. 2019). The viewing angle and BLF of the jet have been taken as roughly the mean of the other jets in the sample, i.e., $1.^\circ35$ and 18, respectively. Within the flares analyzed a doubling time of approximately 0.1 days is observed. This, in conjunction with the assumed Doppler factor, constrains the radius of the emission to less than 3.2×10^{15} cm. The accretion disk luminosity is taken as $2 \times 10^{45}\,{\rm erg\,s^{-1}}$ (E. Pian et al. 1999).

3.1.4. PKS 1329-049 (Two Flares)

PKS 1329-049, located at a redshift of $z = 2.2$ (D. J. Thompson et al. 1990), exhibits a flux doubling time of approximately 0.4 days within the flares analyzed. The jet viewing angle and BLF are assumed to be the same as those for PKS 1424-41 ($\theta_{\rm jet} = 1.^\circ35$ and $\Gamma_{\rm jet} = 18$). This implies that the spherical emission region must have a radius smaller than 1.0×10^{16} cm.

3.1.5. PKS 0402-362 (One Flare)

PKS 0402-362 is located at a redshift of $z = 1.42$ (D. H. Jones et al. 2009). The viewing angle and BLF of the jet have been assumed in the same manner as for PKS 1329-049 and PKS 1424-41. PKS 0402-362 shows a flux doubling time of 0.2 days, implying a radius smaller than 6.5×10^{15} cm. The mass of the central black hole has been determined as $3.16 \times 10^9\,M_\odot$ (R. Decarli et al. 2011).

3.1.6. CTA 102 (One Flare)

CTA 102 is located at a redshift of $z = 1.03$ (T. R. Monroe et al. 2016) and has a central black hole mass of $8.51 \times 10^8\,M_\odot$ (M. Zamaninasab et al. 2014). It has a jet viewing angle and BLF of $1.^\circ6$ and 21.4, respectively (S. G. Jorstad et al. 2017), which gives a Doppler factor of $\delta = 32$. CTA 102 exhibits a flux doubling time of 0.11 days within the flare sampled here. This implies that the spherical emission region must have a radius smaller than 4.4×10^{15} cm.

3.1.7. 3C 454.3 (One Flare)

3C 454.3 is one of the brightest γ-ray sources in the sky. It is located at a redshift of $z = 0.86$ (M. J. Koss et al. 2022) and has a black hole mass of $1.47 \times 10^9\,M_\odot$ (J. Woo & C. M. Urry 2002). The viewing angle and BLF of the jet have been sourced from S. G. Jorstad et al. (2017) as $0.^\circ7$ and 13.8, respectively, making it the most closely aligned jet in the sample. This yields a Doppler factor of $\delta = 27$. The accretion disk luminosity is assumed to be $1.7 \times 10^{47}\,{\rm erg\,s^{-1}}$ (C. M. Raiteri et al. 2008). Within the flare studied here, 3C 454.3 shows a flux doubling time on the order of approximately 1 day. At other times, however, variability on the order of 2 hr has been observed in the optical band (Z. R. Weaver et al. 2019). This implies that the spherical emission region must have a radius smaller than 3.1×10^{15} cm.

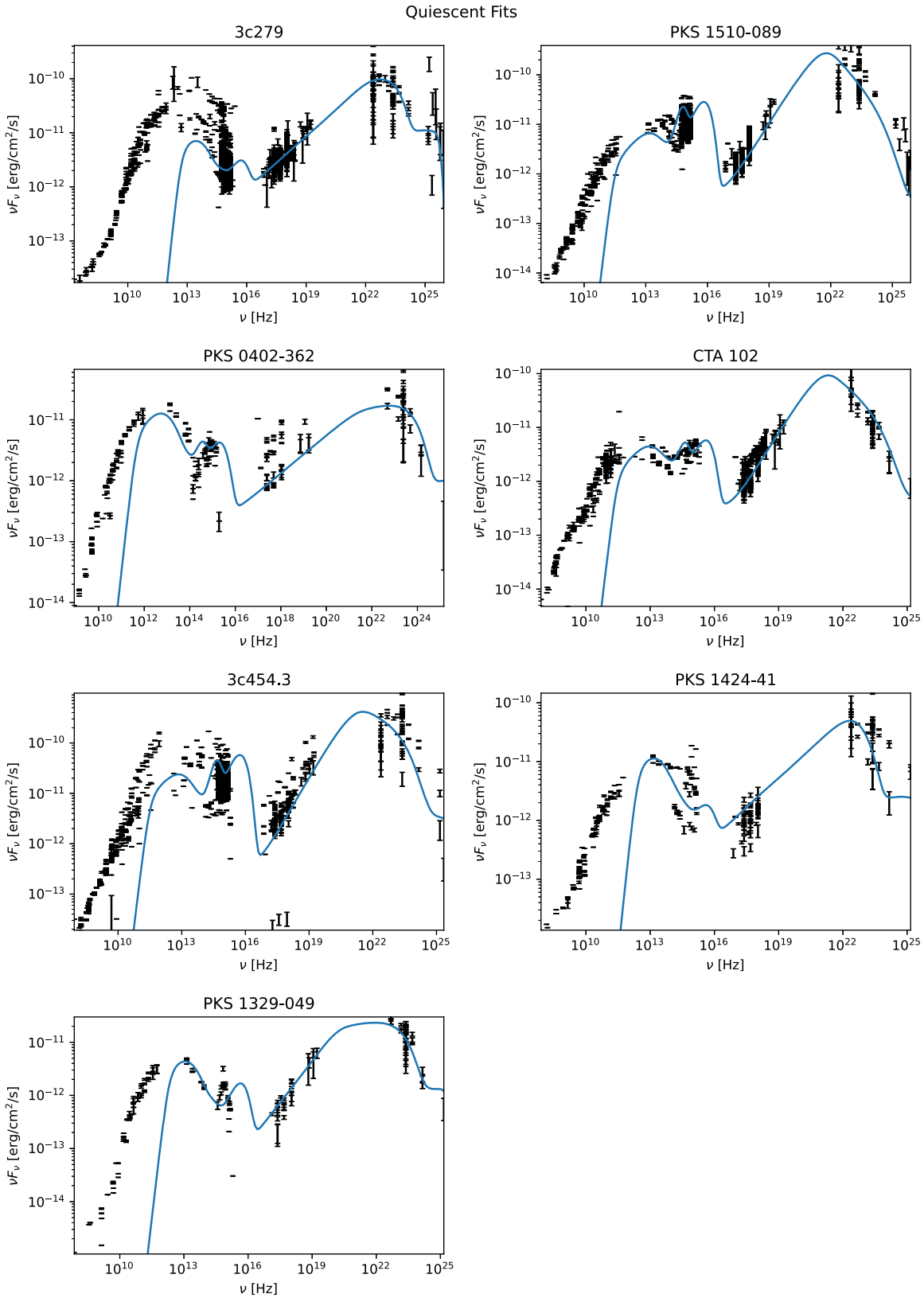


Figure 1. Lepto-hadronic fits for each source in our sample in their quiescent state. See Table 1 for parameters.

4. Results

The quiescent-state fits found for each blazar in the M. Kreter et al. (2020) sample are shown in Figure 1, with their associated parameter sets listed in Table 1. For each flare, the respective source's quiescent state was perturbed in order to reproduce the Fermi-LAT light curve as well as the SED at the point of maximal flux. An example of one of these fits is shown in Figure 2, with the original dates from M. Kreter et al. (2020)

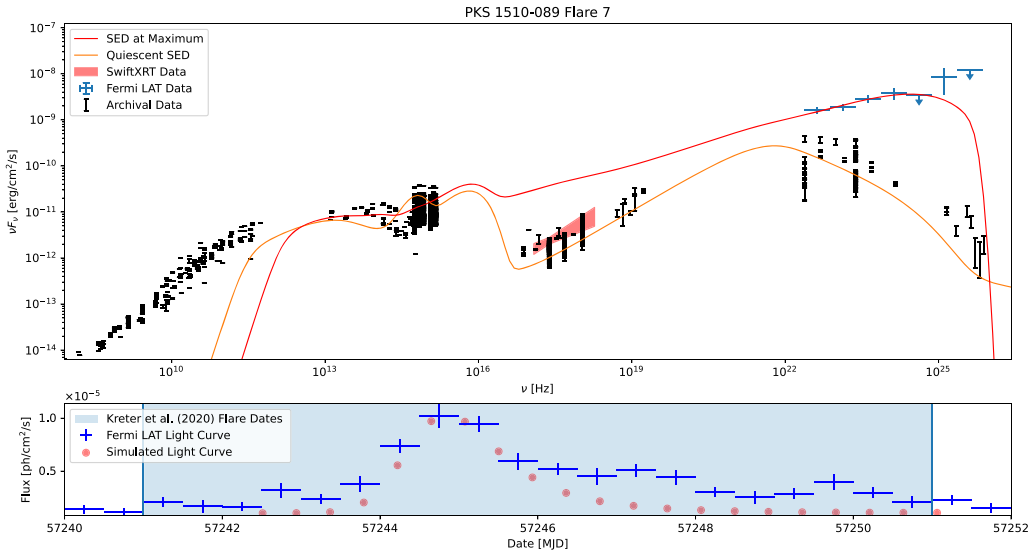


Figure 2. An example of a fit SED and light curve for a flaring event (flare 7) of PKS 1510-089. In the top panel, the quiescent SED fit is shown in orange and the SED fit at the peak of the flare is shown in red. The photon-flux light curve from Fermi-LAT is shown in the bottom panel in blue, along with the simulated light curve in red.

Table 1
Parameters for Quiescent SED Fits Using OneHaLe

	Units	PKS 1510-089	3C 279	PKS 0402-362	CTA 102	3C 454.3	PKS 1424-41	PKS 1329-049
z	⋯	0.4	0.5	1.4	1.0	0.9	1.5	2.1
$M_{\rm bh}$	$(10^8 M_\odot)$	4.5	2.7	31.6	8.5	14.7	4.0	4.0
B	(G)	70	150	70	80	150	100	100
$R_{\rm blob}$	(cm)	4.0×10^{15}	1.0×10^{15}	4.0×10^{15}	3.0×10^{15}	2.0×10^{15}	5.0×10^{15}	5.0×10^{15}
Γ	⋯	22.5	13.3	18.0	21.4	13.8	18.0	18.0
$\theta_{\rm jet}$	(deg)	2.1×10^{-2}	3.3×10^{-2}	2.4×10^{-2}	2.8×10^{-2}	1.2×10^{-2}	2.4×10^{-2}	2.4×10^{-2}
δ	⋯	36.8	22.3	30.5	31.5	26.8	30.5	30.5
z_0	(cm)	1.7×10^{18}	7.8×10^{17}	3.5×10^{18}	2.8×10^{18}	7.2×10^{18}	2.1×10^{18}	3.7×10^{18}
$\frac{\eta R}{c}$	⋯	5	6	5	4	5	3	3
$\frac{\rm acc}{\rm esc}$	⋯	5.0	1.2	5.0	2.5	2.2	2.0	2.0
p_e	⋯	2.9	3.5	3.8	2.9	3.3	3.5	3.8
$\gamma_{{\rm min},e}$	⋯	42	50	47	43	34	50	50
$\gamma_{{\rm max},e}$	⋯	1.0×10^6	1.0×10^6	1.0×10^6	1.0×10^6	1.0×10^6	1.0×10^9	1.0×10^9
L_e	$(\frac{\rm erg}{\rm s})$	7.0×10^{39}	1.3×10^{41}	8.8×10^{41}	1.0×10^{41}	8.0×10^{41}	8.2×10^{41}	7.3×10^{41}
p_p	⋯	1.7	2.2	2.4	1.7	1.5	2.3	1.7
$\gamma_{{\rm min},p}$	⋯	100.1	10.1	100.1	1.1	1.1	1.1	1.1
$\gamma_{{\rm max},p}$	⋯	3.0×10^7	6.0×10^7	3.2×10^8	3.0×10^7	3.0×10^7	1.0×10^8	1.0×10^7
L_p	$(\frac{\rm erg}{\rm s})$	1.4×10^{43}	7.5×10^{44}	4.4×10^{45}	3.0×10^{44}	3.5×10^{44}	5.9×10^{45}	3.6×10^{44}
$\frac{L}{L_{\rm Edd}}$	⋯	1.7×10^{-1}	5.7×10^{-2}	1.0×10^{-1}	2.3×10^{-1}	8.9×10^{-1}	2.9×10^{-1}	8.7×10^{-1}
$R_{\rm blr}$	(cm)	3.2×10^{17}	1.4×10^{17}	6.4×10^{17}	5.0×10^{17}	1.3×10^{18}	3.9×10^{17}	6.7×10^{17}
$L_{\rm blr}$	$(\frac{\rm erg}{\rm s})$	1.0×10^{45}	2.0×10^{44}	4.1×10^{45}	2.5×10^{45}	1.7×10^{46}	1.5×10^{45}	4.6×10^{45}
$T_{\rm blr}$	(K)	10,000	10,000	10,000	10,000	10,000	10,000	10,000
$R_{\rm DT}$	(cm)	3.2×10^{18}	1.4×10^{18}	6.4×10^{18}	5.0×10^{18}	1.3×10^{19}	3.9×10^{18}	6.7×10^{18}
$L_{\rm DT}$	$(\frac{\rm erg}{\rm s})$	1.0×10^{45}	2.0×10^{44}	4.1×10^{45}	2.5×10^{45}	1.7×10^{46}	1.5×10^{45}	4.6×10^{45}
$T_{\rm DT}$	(K)	2000	2000	2000	2000	2000	2000	2000

marked by the shaded region in the light-curve plot. Table 2 shows the parameters for each flare, as well as the total neutrino counts for both IceCube and KM3NeT. Flares 1, 22, and 35 were excluded from this due to difficulties in fitting: attempts to model flares 1 and 22 both produced extremely high optical to X-ray fluxes, caused by runaway pair production. Once flare 35 was analyzed with subday binning, the Fermi-LAT light curve was found to be unusable for this type of study due to the lack of a discernible flaring event during the dates specified in M. Kreter et al. (2020).

The analysis showed that the expected IceCube neutrino counts, as shown in Figure 3, fall below the results from M. Kreter et al. (2020), with most counts leading to a probability of detection of less than 1%. However, when using

Table 2
Parameters For the Additional Proton Power-law Injections for the Modeled Flares

Flare	Source	$\gamma_{\min}$	$\gamma_{\max}$	α	L_p ($\frac{\text{erg}}{\text{s}}$)	Δt (days)	N_ν^{IceCube}	$P_{\text{Det}}^{\text{IceCube}}$ %	N_ν^{KM3NeT}	$P_{\text{Det}}^{\text{KM3NeT}}$ %
2	PKS 1510-089	1.0×10^{2}	2.5×10^{8}	1.7	5.6×10^{44}	5.29	1.1×10^{-3}	0.114	1.5×10^{-2}	1.509
3	PKS 1510-089	1.0×10^{6}	1.5×10^{8}	2.5	2.8×10^{44}	4.8	3.6×10^{-3}	0.362	4.3×10^{-2}	4.229
4	PKS 1510-089	1.0×10^{3}	1.0×10^{8}	1.7	1.2×10^{44}	2.15	5.1×10^{-4}	0.051	6.7×10^{-3}	0.669
5	3C 279	1.0×10^{1}	1.0×10^{8}	1.2	2.8×10^{44}	1.28	1.3×10^{-3}	0.134	2.0×10^{-2}	1.933
6	3C 279	3.0×10^{7}	4.0×10^{7}	1.2	3.1×10^{44}	3.76	5.6×10^{-3}	0.559	8.4×10^{-2}	8.071
7	PKS 1510-089	1.0×10^{2}	3.0×10^{9}	2.3	1.8×10^{45}	7.16	2.2×10^{-3}	0.218	2.7×10^{-2}	2.695
8	3C 279	1.0×10^{1}	1.0×10^{7}	1.3	9.6×10^{44}	3.54	6.5×10^{-3}	0.644	8.1×10^{-2}	7.771
9	PKS 1510-089	1.0×10^{7}	1.0×10^{8}	2.7	3.6×10^{43}	3.77	8.1×10^{-4}	0.081	1.1×10^{-2}	1.087
10	PKS 1510-089	1.0×10^{7}	2.0×10^{8}	2.7	4.0×10^{43}	2.4	5.7×10^{-4}	0.057	7.8×10^{-3}	0.781
11	PKS 1510-089	1.0×10^{7}	1.0×10^{8}	2.9	3.1×10^{43}	1.27	3.1×10^{-4}	0.031	4.2×10^{-3}	0.421
12	PKS 1510-089	1.0×10^{2}	6.0×10^{7}	1.7	1.7×10^{44}	3.38	8.6×10^{-4}	0.086	1.1×10^{-2}	1.109
13	PKS 1510-089	1.0×10^{2}	2.0×10^{8}	2.0	5.1×10^{43}	1.81	2.9×10^{-4}	0.029	3.7×10^{-3}	0.37
14	PKS 1510-089	1.0×10^{7}	1.0×10^{9}	2.8	4.1×10^{43}	1.96	3.6×10^{-4}	0.036	4.7×10^{-3}	0.468
15	PKS 1510-089	1.0×10^{2}	1.5×10^{8}	2.2	4.1×10^{44}	3.02	4.9×10^{-4}	0.049	6.2×10^{-3}	0.614
16	PKS 1510-089	1.0×10^{5}	2.0×10^{9}	2.3	2.4×10^{44}	4.27	7.0×10^{-4}	0.07	8.7×10^{-3}	0.868
17	PKS 1510-089	1.0×10^{2}	2.0×10^{8}	1.7	6.0×10^{42}	2.01	2.9×10^{-4}	0.029	3.7×10^{-3}	0.366
18	PKS 1510-089	1.0×10^{2}	8.0×10^{7}	1.7	5.2×10^{43}	2.95	5.2×10^{-4}	0.052	6.6×10^{-3}	0.662
19	PKS 1510-089	1.0×10^{4}	5.0×10^{7}	2.0	5.1×10^{43}	27.44	6.4×10^{-3}	0.638	8.0×10^{-2}	7.658
20	PKS 1510-089	1.0×10^{6}	1.0×10^{7}	2.0	1.3×10^{44}	9.3	4.2×10^{-3}	0.415	4.7×10^{-2}	4.564
21	PKS 1510-089	1.0×10^{2}	4.0×10^{8}	2.5	1.8×10^{46}	5.76	5.2×10^{-3}	0.522	7.1×10^{-2}	6.828
23	PKS 1510-089	1.0×10^{2}	3.0×10^{8}	1.7	9.3×10^{42}	0.45	7.1×10^{-5}	0.007	9.1×10^{-4}	0.091
24	PKS 1510-089	1.0×10^{2}	7.0×10^{7}	1.7	3.1×10^{43}	3.11	5.3×10^{-4}	0.053	6.7×10^{-3}	0.666
25	PKS 1510-089	1.0×10^{2}	1.0×10^{8}	1.7	4.7×10^{43}	2.43	4.3×10^{-4}	0.043	5.5×10^{-3}	0.547
26	PKS 1510-089	1.0×10^{6}	1.0×10^{8}	1.1	1.2×10^{43}	1.28	2.0×10^{-4}	0.02	2.5×10^{-3}	0.25
27	3C 279	1.0×10^{1}	6.0×10^{7}	2.0	1.1×10^{45}	1.89	1.5×10^{-3}	0.15	2.1×10^{-2}	2.089
28	PKS 0402-362	3.2×10^{7}	3.2×10^{8}	3.0	2.0×10^{45}	2.98	1.5×10^{-4}	0.015	2.3×10^{-3}	0.226
29	PKS 1510-089	1.0×10^{2}	8.0×10^{7}	1.7	1.9×10^{43}	2.14	3.5×10^{-4}	0.035	4.4×10^{-3}	0.438
30	PKS 1510-089	1.0×10^{2}	1.0×10^{8}	1.7	2.0×10^{43}	1.71	2.9×10^{-4}	0.029	3.8×10^{-3}	0.375
31	CTA 102	1.1	4.0×10^{8}	2.5	1.5×10^{24}	2.44	5.5×10^{-3}	0.545	6.6×10^{-2}	6.421
32	3C 279	1.0×10^{6}	7.5×10^{7}	2.2	3.1×10^{44}	4.56	1.4×10^{-3}	0.144	2.0×10^{-2}	2.018
33	PKS 1510-089	1.0×10^{2}	1.0×10^{8}	1.7	2.0×10^{43}	1.34	2.4×10^{-4}	0.024	3.2×10^{-3}	0.315
34	3C 279	1.0×10^{1}	6.0×10^{8}	2.0	7.1×10^{44}	5.38	6.1×10^{-3}	0.607	8.6×10^{-2}	8.281
36	3C 279	1.0×10^{7}	1.0×10^{8}	1.8	1.6×10^{44}	5.91	2.1×10^{-3}	0.205	2.9×10^{-2}	2.895
37	PKS 1510-089	1.0×10^{2}	9.0×10^{7}	2.4	2.2×10^{46}	1.64	1.1×10^{-3}	0.11	1.4×10^{-2}	1.426
38	3C 454.3	1.1	1.0×10^{8}	1.5	6.1×10^{44}	127.05	1.4×10^{-2}	1.4	1.9×10^{-1}	17.124
39	PKS 1510-089	1.0×10^{1}	1.0×10^{8}	2.4	2.2×10^{46}	1.74	1.3×10^{-3}	0.13	1.6×10^{-2}	1.612
40	PKS 1510-089	1.0×10^{2}	8.0×10^{7}	2.0	1.2×10^{44}	2.85	5.8×10^{-4}	0.058	7.3×10^{-3}	0.731
41	PKS 1424-41	1.1	6.0×10^{8}	2.4	5.3×10^{47}	2.65	1.4×10^{-4}	0.014	2.4×10^{-3}	0.236
42	3C 279	1.0×10^{1}	1.0×10^{7}	2.0	2.9×10^{45}	1.51	4.0×10^{-3}	0.402	5.2×10^{-2}	5.111
43	PKS 1424-41	1.1	6.0×10^{8}	2.3	9.8×10^{46}	2.81	1.2×10^{-4}	0.012	1.8×10^{-3}	0.182
44	PKS 1510-089	1.0×10^{2}	2.0×10^{8}	2.8	5.4×10^{47}	6.83	1.5×10^{-2}	1.476	3.6×10^{-1}	30.3
45	PKS 1510-089	1.0×10^{2}	8.0×10^{7}	1.7	1.9×10^{43}	3.14	5.6×10^{-4}	0.056	7.2×10^{-3}	0.718
46	PKS 1510-089	1.0×10^{2}	3.0×10^{8}	1.7	2.9×10^{42}	2.06	2.9×10^{-4}	0.029	3.6×10^{-3}	0.364
47	PKS 1329-049	1.1	1.0×10^{7}	1.0	1.0×10^{26}	1.07	2.7×10^{-3}	0.27	3.1×10^{-2}	3.066
48	PKS 1329-049	1.1	1.0×10^{7}	1.5	2.1×10^{26}	1.87	2.4×10^{-3}	0.236	2.7×10^{-2}	2.669
49	PKS 1424-41	1.1	9.0×10^{8}	1.5	5.4×10^{44}	1.83	1.8×10^{-5}	0.002	2.6×10^{-4}	0.026
50	PKS 1510-089	1.0×10^{2}	1.0×10^{7}	2.0	4.6×10^{44}	3.37	1.1×10^{-3}	0.113	1.3×10^{-2}	1.294

Notes. The last four columns list the expected numbers of neutrinos to be detected by IceCube and KM3NeT and the Poissonian probability of detection.

the effective areas for KM3NeT, the probability of detection reaches nearly 10% in some cases.

As all fitting of the perturbation parameters was done by eye and there are substantial parameter degeneracies, the chosen set of parameters for each flare is not unique and may not be the one that maximizes the expected neutrino detection rate. In order to investigate the impact of these parameter degeneracies on the predicted neutrino detection rates, a grid scan was performed on two of the flares, namely flare 21 and flare 34. Grid scans were used, as exploring the parameter spaces fully was prohibitively expensive in terms of computational times. The results of both grid scans are included in Figure 3, with the results of all acceptable simulations presented in blue and orange. This revealed that the maximum and minimum neutrino counts do not differ by more than roughly 1 order of magnitude. This implies that, while each set of parameters may not necessarily represent the most optimistic neutrino prediction, the results presented do give an accurate indication of neutrino expectations. Flare 38, a month-long outburst from 3C 454.3, stands out within the sample as not only being the longest flare in the sample but also producing the most neutrinos as a result of this length. The fitting in this work was only able to recreate the long-term behavior of this flare, and as such, the true level of neutrino production may be even higher if the short-term behavior is included.

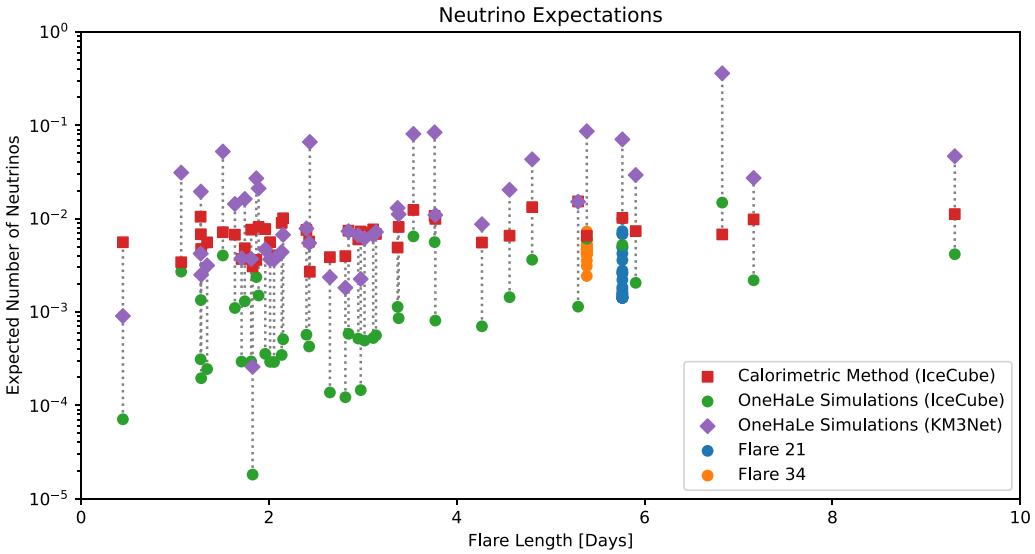


Figure 3. Neutrino count expectations for OneHaLe simulations of the sample of blazar flares. Expected counts for the IceCube Neutrino Observatory are shown in green, and those for KM3NeT are shown in purple. The expected neutrino counts using the calorimetric method are shown in red. The orange and blue dots represent the results from the grid scans of flare 34 and flare 21, respectively.

5. Summary and Discussion

In this work, we have modeled the flares of seven different blazars. Using a time-dependent lepto-hadronic code the steady-state quiescent solutions were perturbed to recreate the flare light cures as well as the SEDs during the flares. The neutrino flux produced during each of these flares was then convolved with the effective areas of the IceCube Neutrino Observatory and KM3NeT to calculate the expected neutrino counts for each detector during the flares. From the total neutrino counts, the probability of a positive detection (the probability of observing one or more neutrinos) was then calculated by treating the counts calculated above as the mean event rate in a Poisson distribution. This analysis showed that, of the flares modeled, IceCube was unlikely to have made a definitive detection of any of the blazars as a point source. As many of the flares had a detection probability of less than 1% the nondetection of these blazars, even while in a flaring state, is the most probable result. These results therefore support the results and conclusions of M. Kreter et al. (2020) as, for most flares, the neutrino counts are overestimated by the calorimetric method by only a small factor. For the KM3NeT detector, however, the results are more promising, with the detection probability of many flares being on the order of $\sim$10%. This implies that with multiple flares each year the probability of detecting a neutrino from these sources is high over extended periods of time.

5.1. Limitations

The flares here are sourced from M. Kreter et al. (2020), which used daily binning for light curves, therefore excluding subday length flares. Furthermore, the fits presented in this work represent only one of a number of degenerate parameter choices and do not necessarily maximize the neutrino detection predictions. Separate fits may be found, even within a different parameter regime (for example, one with the high energy emission being produced by inverse-Compton radiation with only a subdominant hadronic component). The analysis performed using grid scans has, however, shown that if the high-energy emission is hadronically dominated, our predictions are expected to be accurate within 1 order of magnitude.

The flares are also being modeled with very simple perturbations from the quiescent state, whereas in reality, flares may be a result of much more complex processes, possibly leading to different neutrino predictions. Some of our flare fit attempts produced excessive emission in the optical–UV bands due to pγ-induced pair cascades of magnitudes, which are not seen in archival data for these sources. This shows that while these simple models for the flaring states can reproduce the spectral and temporal changes seen in γ-rays, future simultaneous optical–UV observations are required to verify or rule out a hadronically dominated model for blazar flares.

6. Conclusions

This work has shown that even in a flaring state the sampled blazars do not produce neutrinos in high enough quantities to lead to definitive detection using current-generation neutrino observatories, in particular, IceCube. This is consistent with other work such as K. Yoshida et al. (2023) and indicates that while the presence of neutrinos from blazar jets cannot be ruled out, it is unlikely that they are predominantly the source of high-energy cosmic neutrinos, though they may still contribute a notable fraction. The projections for KM3NeT neutrino counts show promise that future detectors may indeed be able to detect more individual blazars as neutrino point sources.

Our work shows that the calorimetric method, while overestimating the amount of neutrinos produced by a factor of $\sim$10, still holds for the general trend of flaring proton-synchrotron blazars. If the empirical factor is adjusted accordingly then this method presents a much faster way of estimating neutrino expectations from flaring blazars than physical modeling.

Acknowledgments

This work was supported by the Department of Science and Innovation and the National Research Foundation of South Africa through the South African Gamma-Ray Astronomy

Programme (SA-GAMMA). J.B. is supported by the National Astrophysics and Space Science Programme (NASSP).

ORCID iDs

Joshua Robinson https://orcid.org/0000-0001-6399-3001
Markus Böttcher https://orcid.org/0000-0002-8434-5692

References

Aartsen, M., Ackermann, M., Adams, J., et al. 2018, Sci, 361, eaat1378
Aartsen, M. G., Abbasi, R., Abdou, Y., et al. 2013, Sci, 342, 1242856
Abbasi, R., Ackermann, M., Adams, J., et al. 2022, Sci, 378, 538
Abdollahi, S., Acero, F., Ackermann, M., et al. 2020, ApJS, 247, 33
Acharyya, A., Adams, C. B., Archer, A., et al. 2023, ApJ, 954, 70
Adrián-Martinez, S., Ageron, M., Aharonian, F., et al. 2016, JPhG, 43, 084001
Bottcher, M., Harris, D. E., & Krawczynski, H. 2012, Relativistic Jets from Active Galactic Nuclei (Berlin: Wiley)
Buson, S., Tramacere, A., Pfeiffer, L., et al. 2022, ApJL, 933, L43
Cerruti, M. 2020, Galax, 8, 72
Decarli, R., Dotti, M., & Treves, A. 2011, MNRAS, 413, 39
Diltz, C., & Böttcher, M. 2016, ApJ, 826, 54
Gaisser, T. K., Halzen, F., & Stanev, T. 1996, PhR, 271, 355
Garrappa, S., Buson, S., Franckowiak, A., et al. 2019, ApJ, 880, 103
Ghisellini, G., & Ghisellini, G. 2013, LNP, 873, 1
Ghisellini, G., & Tavecchio, F. 2009, MNRAS, 397, 985
Hillas, A. M., & Hillas, M. A. 1984, ARA&A, 22, 425
Jones, D. H., Read, M. A., Saunders, W., et al. 2009, MNRAS, 399, 683
Jorstad, S. G., Marscher, A. P., Morozova, D. A., et al. 2017, ApJ, 846, 98
Kadler, M., Krauß, F., Mannheim, K., et al. 2016, NatPh, 12, 807
Koss, M. J., Ricci, C., Trakhtenbrot, B., et al. 2022, ApJS, 261, 2
Krauß, F., Kadler, M., Mannheim, K., et al. 2014, A&A, 566, L7
Kreter, M., Kadler, M., Krauß, F., et al. 2020, ApJ, 902, 133
Mannheim, K., & Biermann, P. L. 1992, A&A, 253, L21
Marziani, P., Sulentic, J. W., Dultzin-Hacyan, D., Calvani, M., & Moles, M. 1996, ApJS, 104, 37
Monroe, T. R., Prochaska, J. X., Tejos, N., et al. 2016, AJ, 152, 25
Murase, K., Oikonomou, F., & Petropoulou, M. 2018, ApJ, 865, 124
Murphy, M. T., Kacprzak, G. G., Savorgnan, G. A. D., & Carswell, R. F. 2019, MNRAS, 482, 3458
Pian, E., Falomo, R., & Treves, A. 2005, MNRAS, 361, 919
Pian, E., Urry, C. M., Maraschi, L., et al. 1999, ApJ, 521, 112
Plavin, A., Kovalev, Y. Y., Kovalev, Y. A., & Troitsky, S. 2020, ApJ, 894, 101
Plavin, A. V., Kovalev, Y. Y., Kovalev, Y., & Troitsky, S. V. 2021, ApJ, 908, 157
Plavin, A. V., Kovalev, Y. Y., Kovalev, Y. A., & Troitsky, S. V. 2023, MNRAS, 523, 1799
Pucella, G., Vittorini, V., D'Ammando, F., et al. 2008, A&A, 491, L21
Raiteri, C. M., Villata, M., Larionov, V. M., Gurwell, M. A., & Chen, W. P. 2008, A&A, 491, 755
Sahakyan, N., Giommi, P., Padovani, P., et al. 2023, MNRAS, 519, 1396
Seyfert, C. K. 1943, ApJ, 97, 28
Thompson, D. J., Djorgovski, S., & de Carvalho, R. 1990, PASP, 102, 1235
Verner, D. A., Ferland, G. J., Korista, K. T., & Yakovlev, D. G. 1996, ApJ, 465, 487
Weaver, Z. R., Balonek, T. J., Jorstad, S. G., et al. 2019, ApJ, 875, 15
Wilms, J., Allen, A., & McCray, R. 2000, ApJ, 542, 914
Woo, J.-H., & Urry, C. M. 2002, ApJ, 579, 530
Wood, M., Caputo, R., Charles, E., et al. 2018, PoS, 301, 824
Yoshida, K., Petropoulou, M., Murase, K., & Oikonomou, F. 2023, ApJ, 954, 194
Zacharias, M. 2021, Physi, 3, 1098
Zacharias, M., Reimer, A., Boisson, C., & Zech, A. 2022, MNRAS, 512, 3948
Zamaninasab, M., Clausen-Brown, E., Savolainen, T., & Tchekhovskoy, A. 2014, Natur, 510, 126